



HIGHLANDER
HIGH performing uLtrA-durable membraNe electroDe assEmblies for tRucks

HIGH PERFORMING ULTRA-DURABLE MEMBRANE ELECTRODE ASSEMBLIES FOR TRUCKS

Grant agreement no.: 101101346

Start date: 01.01.2023 – **Duration:** 36 months

Project Coordinator: D. J. Jones, CNRS

The HIGHLANDER project is supported by the Clean Hydrogen Partnership and its members Hydrogen Europe and Hydrogen Europe Research.

Views and opinions expressed are however those of the author(s) only and do not necessarily reflect those of the European Union or Clean Hydrogen JU. Neither the European Union nor the granting authority can be held responsible for them.

DELIVERABLE REPORT

D5.1: DESCRIPTION OF DEVELOPED EX-SITU FUNCTIONAL CHARACTERISATION TECHNIQUES		
Due Date	31 March 2024	
Author (s)	Peter Lindner	
Workpackage	WP5 Innovative Lower Cost GDL	
Workpackage Leader	Thilo Lehre	
Lead Beneficiary	Bosch	
Date released by WP leader	22/02/2024	
Date released by Coordinator	22/02/2024	
DISSEMINATION LEVEL		
PU	Public	X
SEN	Sensitive, limited under the conditions of the Grant Agreement;	
NATURE OF THE DELIVERABLE		
R	Document, report	X
DEM	Prototype demonstrator	
DEC	Website	
DMP	Data management plan	
OTHER	Software, algorithms, models	

SUMMARY	
Keywords	Innovative Lower Cost GDL; convective Transport; contact resistance; specific conductivity.
Abstract	<p>The proton-exchange membrane fuel cell (PEMFC) is a promising low-temperature fuel cell for CO₂ neutral electrification of vehicles. However, marketability requires reduced stack cost and improved lifetime. One costly component is the gas diffusion layer (GDL). The task of reducing GDL cost requires measuring the important physical GDL properties, so that they can be optimised both in terms of cost and function.</p> <p>This report describes the development of measurement methods of physical GDL properties for convective transport, electrical bulk conductivity and contact resistance.</p>
Public abstract for confidential deliverables	<p>The proton-exchange membrane fuel cell (PEMFC) is a promising low-temperature fuel cell for CO₂ neutral electrification of vehicles. However, marketability requires reduced stack cost and improved lifetime. One costly component is the gas diffusion layer (GDL). The task of reducing GDL cost requires measuring the important physical GDL properties, so that they can be optimised both in terms of cost and function.</p> <p>This report describes the development of measurement methods of physical GDL properties for convective transport, electrical bulk conductivity and contact resistance.</p>

REVISIONS			
Version	Date	Changed by	Comments
0.1	07.02.2024	P. Lindner	

DELIVERABLE TITLE

CONTENTS

1	Introduction.....	4
2	Ex-situ functional GDL characterisation techniques	5
2.1	Permeability characterisation technique.....	5
2.2	Specific in-plane conductivity and contact resistance characterisation technique	12
2.3	Through-plane resistance measurement method	18
3	Conclusions and future work.....	19
4	References.....	19

1 INTRODUCTION

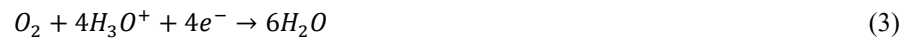
The proton-exchange membrane fuel cell (PEMFC) is a promising low-temperature fuel cell for CO₂ neutral electrification of vehicles. However, marketability requires reduced stack cost and improved lifetime. The principle of the fuel cell is based on oxidation of hydrogen:



which is divided into the anode reaction,



and the cathode reaction.



A principal structure of the fuel cell can be seen in Figure 1. [1]

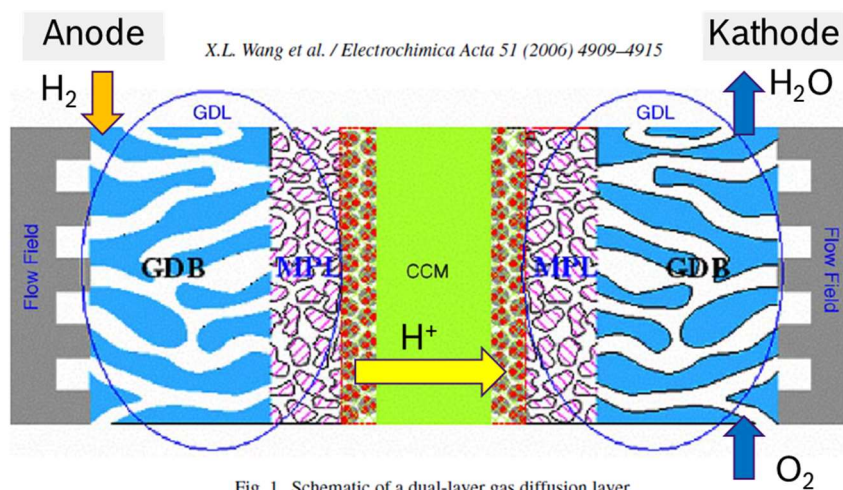


Fig. 1. Schematic of a dual-layer gas diffusion layer.

Figure 1: Schematic image of a PEMFC [1].

On the anode side, hydrogen is homogeneously distributed by the flow field, the gas diffusion layer (GDL) consisting of a gas diffusion backing (GDB) and the micro-porous layer (MPL). The reaction described in Equation 2 takes place at the triple-phase boundary in the catalyst layer coated on the proton exchange membrane (CCM). The protons from anodic hydrogen oxidation are transported through the CCM to the cathode side, where they then react with the oxygen to form water (Equation 3). On the cathode side, there is also a GDL and flow field for the homogeneous distribution of oxygen and the transport of water. In addition, the flow field and GDL structures have besides a mechanical function also the function of conducting the electrical current and conducting the generated heat.

As can be seen from Equations 1-3 and Figure 1, gas and water transport is one of the key processes in the PEMFC [1] [2] [3] strongly depending on diffusive as well as convective behavior of the porous GDL structure. Especially low oxygen transport rates can limit high current oxygen reduction rates at the triple phase boundary. One reason for low oxygen transport can be blockage of GDL pores with liquid water. On the other hand, high water removal rates can lead to membrane dry out and in turn to reduced proton conductivity. Other important physical GDL properties are electrical bulk conductivity and contact resistance as they determine ohmic losses lowering fuel cell efficiency.

This report describes the development of measurement methods of physical GDL properties for convective transport, electrical conductivity and contact resistance.

2 EX-SITU FUNCTIONAL GDL CHARACTERISATION TECHNIQUES

2.1 Permeability characterisation technique

This section describes the experimental determination of convective transport within gas diffusion layer (GDL) consisting of backing paper and micro porous layer (MPL), see Figure 1. Microscopic images of these two porous components are shown in Figure 2 [4].

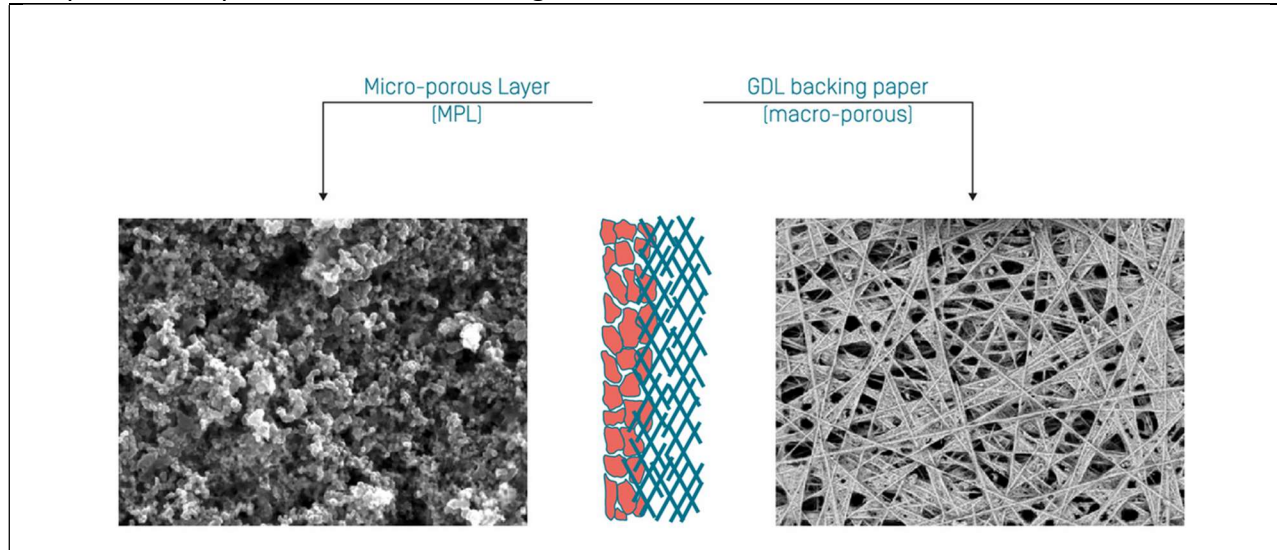


Figure 2: Gas diffusion layer (GDL) with the micro-porous layer (MPL) [4].

Convective gas transport in porous materials is usually described by Darcy's equation (4) [5] [6] [2].

$$\frac{dp}{dx} = -\frac{\eta}{B_v} v \quad (4)$$

This equation describes the pressure drop $\frac{dp}{dx}$ along the porous material due to a medium flowing through at velocity v . η is the viscosity of the gas or fluid and B_v is the permeability. For the one-dimensional case and a homogenous material, B_v is a scalar and has the dimension m^2 . Gravity is not considered in this and subsequent equations. A three-dimensional consideration results in following equation:

$$\nabla p = -\frac{\eta}{B_v} \vec{v} \quad (5)$$

$$\underline{B_v} = \begin{pmatrix} B_{11} & B_{12} & B_{13} \\ B_{21} & B_{22} & B_{23} \\ B_{31} & B_{32} & B_{33} \end{pmatrix} \quad (6)$$

where \vec{v} is a vector of the flow velocity and $\underline{B_v}$ is a second-order symmetric tensor of the permeability. Due to the symmetric properties of permeability, the following equations are valid: $B_{21}=B_{12}$, $B_{13}=B_{31}$, $B_{32}=B_{23}$. When the principal axes for the permeability are parallel to the coordinate axes, the tensor becomes diagonal. That is not true in general. The physical interpretation of the terms is straightforward. B_{ij} is the permeability relating to the velocity in the direction i to the pressure gradient in the direction j . Therefore, when the principal axes are not aligned with the coordinate axis, a pressure gradient in one direction can induce a velocity in a perpendicular direction [7].

Due to very different through-plane and in-plane characteristic length scales, GDLs samples are designed to have strong anisotropy for permeability and conductivity introducing oriented carbon fibres. Consequently, B_v is treated here as a tensor not a scalar.

Two extensions of the Darcy equation should be mentioned as well: the Brinkman extension and the Forchheimer extension. For further consideration, please refer to the following literature [6] [2].

Brinkman extension

$$\nabla p = -\frac{\eta}{B_v} \vec{v} + \tilde{\eta} \nabla^2 \vec{v} \quad (7)$$

The second term on the right-hand side is a shear stress term such as would be required by a boundary wall no-slip condition. $\tilde{\eta}$ describes the effective viscosity on the wall. This effect is only significant if the sample thickness reaches the size order of $\sqrt{B_v}$ [2].

Forchheimer extension

$$\nabla p = -\frac{\eta}{B_v} \vec{v} - c_F \sqrt{B_v \rho_g} |\vec{v}| \vec{v} \quad (8)$$

Darcy's equation applies to non-turbulent flows, if the gas velocity is increased, and must be extended by the Forchheimer extension, where c_F is a constant and ρ_g the gas density. The second term on the right side of the equation 8 only plays a role if the gas velocities are high enough. This can be described by the Reynolds number (Equation 9). If the Reynolds number is in the range 1-10 or greater, the Darcy equation must be extended by the Forchheimer term [6] [2].

$$Re_B = \frac{\rho_g v \sqrt{B_v}}{\eta} \quad (9)$$

A good overview of experimental investigations and underlying theory is given in [8]. Characterisation techniques can be constant flow or constant pressure difference:

1. A constant gas flow and thus a constant velocity is set, and the corresponding pressure difference is measured. This is done for different gas flows. The permeability is determined from the slope of the Darcy equation (cf. Equation 4).
2. A constant pressure difference is set, and the corresponding gas flow is measured. This is also done for different gas pressures. The permeability is determined from the gradient (Equation 4).

In this report, all experiments were performed with a constant flow. To determine the anisotropy in the convective transport, both in-plane flow and through-plane flow arrangements have been investigated. The first section describes a through-plane flow arrangement with sample compression and the second section describes an in-plane flow arrangement with sample compression.

2.1.1 Through-plane permeability measurement with sample compression

Figure 3 shows the principle cross section structure for a through-plane flow experiment with sample compression. By using the gas supply and the flow meter, the gas (dry air) is introduced into the sample chamber with the GDL in a controlled manner i.e., a constant volumetric gas flow is set. The absolute pressure and the gas temperature are determined in the inlet flow. The differential pressure is also measured. To determine the permeability using Darcy's equation, the velocity can be calculated from the constant flow.

$$Q_v = v_A A \quad (10)$$

Q_v describes the constant volumetric flow for standard conditions, v_A the flow velocity, $A=\pi d^2/4$ the area of the sample and d is the diameter of the sample. If laboratory conditions are different from standard, laboratory volumetric flows are calculated using Equation 11.

$$Q_N = Q_v \frac{p T_N}{p_N T} \tag{11}$$

where p is the actual pressure and T the actual temperature, p_N is the pressure and T_N is the temperature of the standard conditions (e.g. $p_N=1.01325$ bar and $T_N=273.15$ K). From equations 10 and 11 follows:

$$v_A = Q_N \frac{4 T p_N}{T_N p d^2 \pi} \tag{12}$$

The gas flow is shown in Figure 3 and symbolised by a red arrow. The pressure difference is determined as shown in the drawing. It is essential to perform a measurement without a specimen and to subtract it as "background".

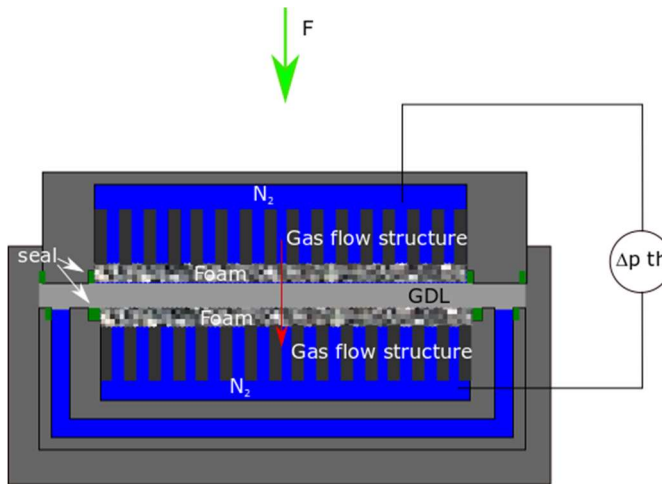


Figure 3: Principle experimental set-up in the through-plane flow arrangement with sample compression.

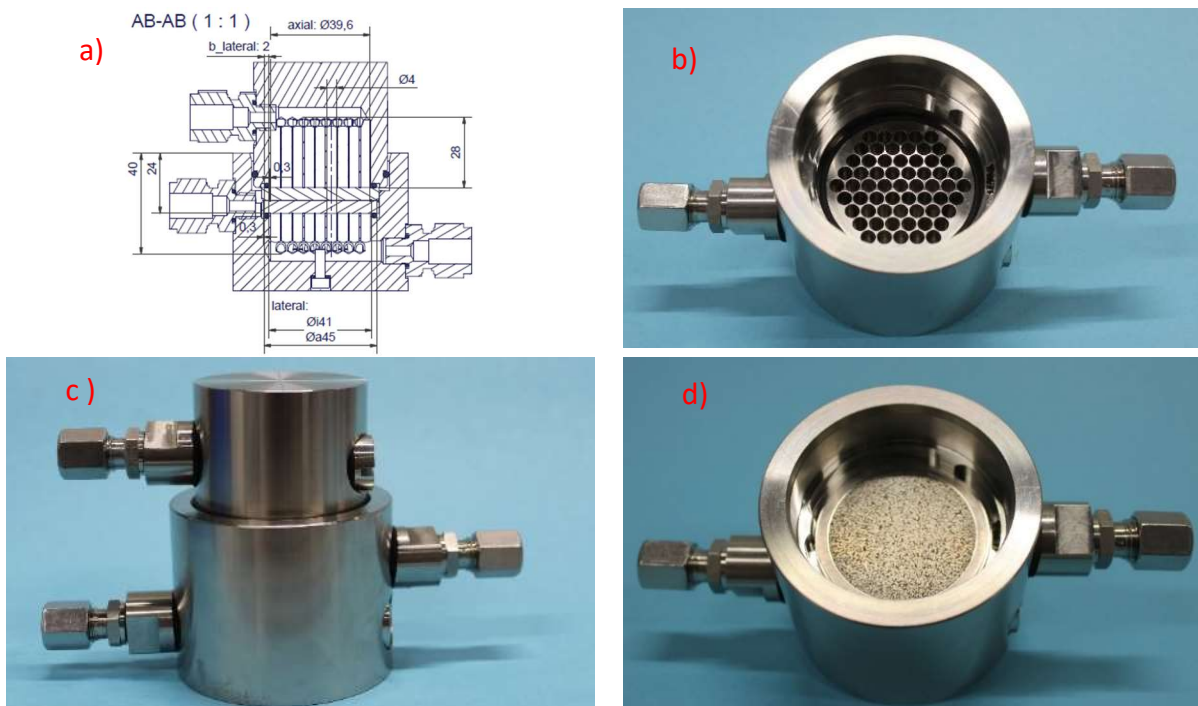


Figure 4: Technical realization of experiments to determine the permeability under mechanical stress.

Figure 4 shows the technical realisation of the experiment: CAD drawing in cross section (4a), coarse structure of the gas supply (4b) and frit on top of the previous structure (4c). It is possible to investigate the permeability as a function of the compression of the sample. The challenge with this setup was on the one hand to ensure gas transport through the specimen and on the other hand to apply mechanical pressure to the specimen. For this purpose, the structure was planned so that the GDL is located between two metallic foams (frit). Mechanical pressure is applied to the frit by an external press, compressing the sample. Above and below the frit, there is a coarser gas distributor structure. Figure 5 shows a prepared sample, which was punched out to the appropriate size.



Figure 5: Sample geometry of a GDL.

Measurement data for constant gas flow is plotted in Figure 6. Figure 6a shows the differential pressure and Figure 6b the volumetric flow rate over time. A constant volumetric flow rate is set and maintained until a constant differential pressure is reached, which is averaged over a time interval indicated by red bars in Figure 6. Subsequently, the gas flow is increased to the next measurement level. From Darcy's equation (Equation 4) follows:

$$\frac{\Delta p}{h} = -\frac{\eta}{B_v} v_A \quad (13)$$

The sample thickness is h and $\Delta p = p_2 - p_1$. In our case $p_2 < p_1$, Δp is negative, and the sign is reversed on the right-hand side of Equation 13. The viscosity of air is $1.85 \cdot 10^{-5}$ Pa/s [9].

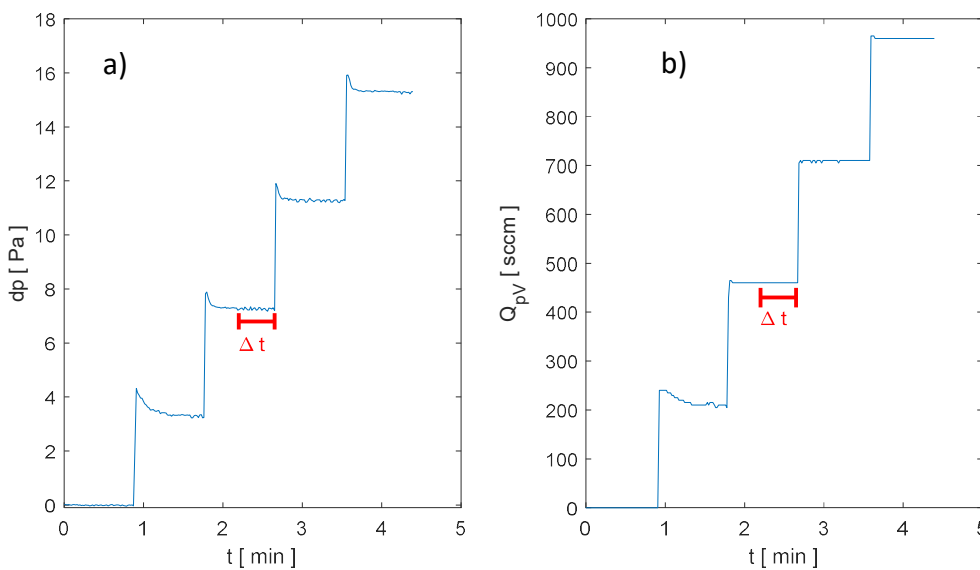


Figure 6: Time trace of pressure difference and volumetric flow rate.

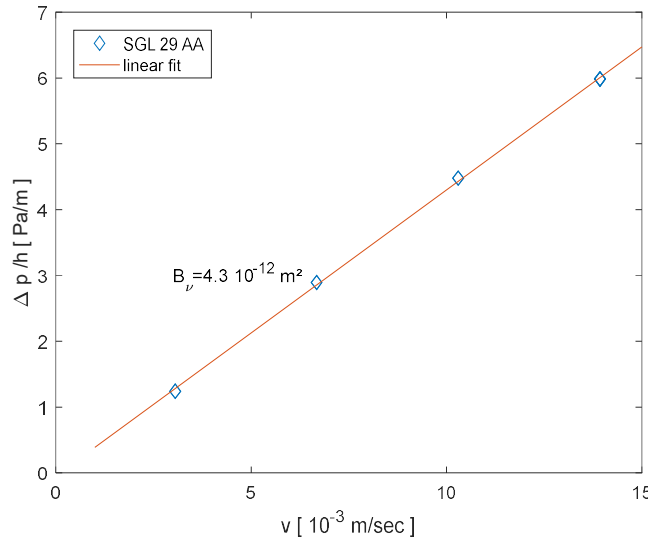


Figure 7: Experimental data for GDL SGL 29 AA.

According to equation 13, the permeability can be determined from the Δp - v slope, see Figure 7. The experimental data for an SGL 29 AA GDL and the linear fit used to determine permeability are shown in Figure 7. Under the measured conditions, no deviation from the linear behavior described in Darcy's equation was determined. The applied force compresses the GDL and reduces GDL porosity and permeability i.e., the sample thickness h is a function of force F or mechanical stress, see equation 15.

$$\frac{\Delta p}{h(F)} = -\frac{\eta}{B_v} v_A \quad (14)$$

The permeability under mechanical stress is calculated using equation 16.

$$\frac{\Delta p}{h_0 C(F)} = -\frac{\eta}{B_v} v_A \quad (15)$$

$C(F)$ is the ratio of compressed (h) to uncompressed (h_0) sample thickness.

$$C(F) = \frac{h}{h_0} \quad (16)$$

2.1.2 Calibration of through-plane permeability measurement method

For the calibration of the experimental device, sintered samples (SIKA R) were used whose permeability is known and which cannot be compressed in the range considered here. Figure 8 shows the result of the calibration. Measured permeabilities correlate reasonably well with the specified permeabilities of the calibration samples. A total of 12 samples are measured, 4 types of samples with different permeabilities and 3 samples of each type. Furthermore, the non-compressibility of the calibration samples is confirmed, Figure 9 showing the pressure independence of the permeability for three samples of one type. Figure 10 shows the reproducibility of experiments in which one sample is measured, removed from the experiment, and measured again. This procedure was repeated five times and reproducibility of results confirmed.

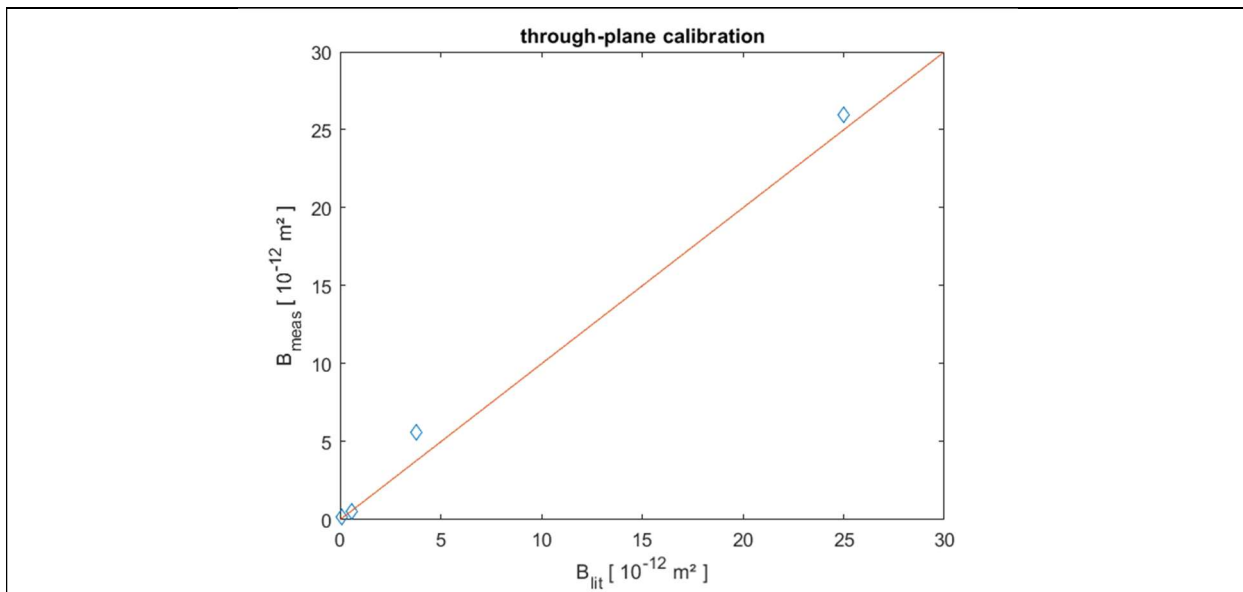


Figure 8: Calibration of the experimental set-up with calibration samples.

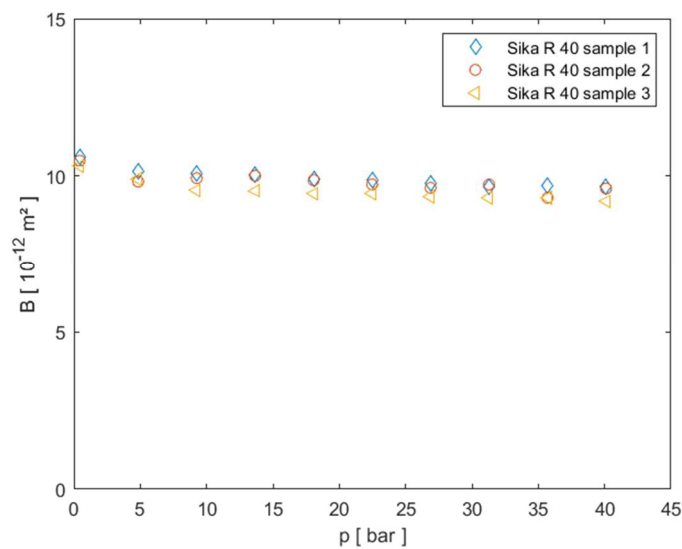


Figure 9: Characterization of three non-compressible calibration samples.

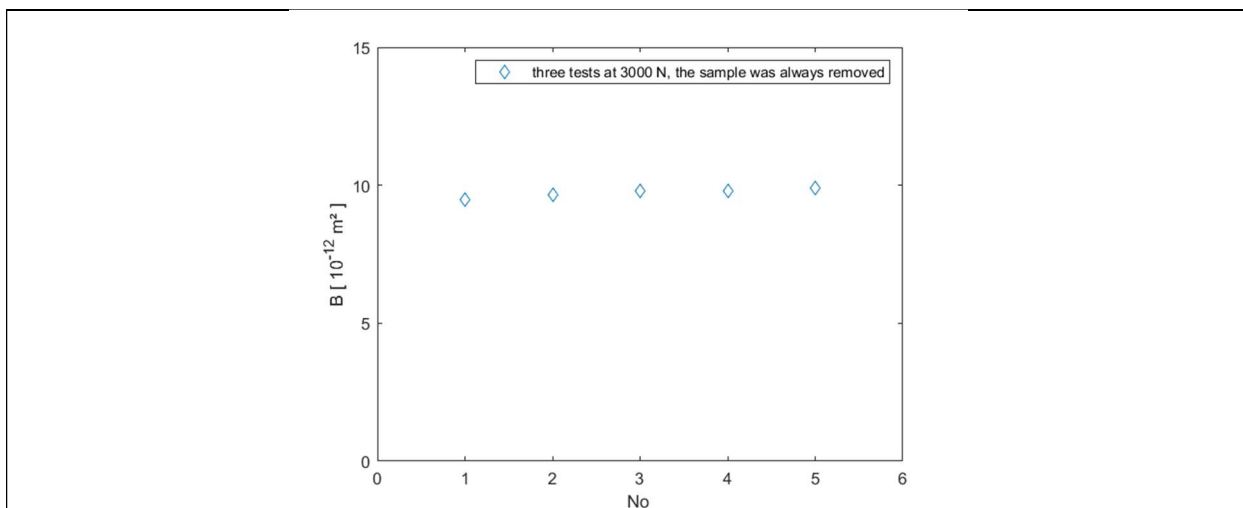


Figure 10: Repeat measurement to investigate the reproducibility of permeability measurements.

2.1.3 In-plane permeability measurement with sample compression

For in-plane permeability measurements under mechanical stress, the above-described experimental setup is used. Two differences are the sample geometry (see Figure 11) and the gas flow (see Figure 12). Due to these two changes, the gas flows through the sample in the plane. The evaluation of the measurement data must be adapted to the gas flow and the sample geometry. The Darcy equation is converted into cylinder coordinates and the sample geometry (ring) is taken into account, the exact derivation can be taken from the literature [10] [11] [12]. The resulting equations are shown below (Equations 19 and 20). It is also necessary to take compressibility into account (see Equation 21).

$$Q_v = \frac{2\pi B_v h}{\eta \ln(r_o/r_i)} \Delta p \tag{17}$$

$$\Delta p = \frac{\eta \ln(r_o/r_i)}{2\pi B_v h} Q_v \tag{18}$$

$$\Delta p = \frac{\eta \ln(r_o/r_i)}{2\pi B_v h_0 C(F)} Q_v \tag{19}$$

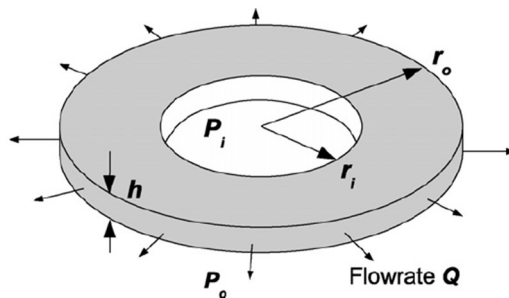


Figure 11: In-plane sample geometry.

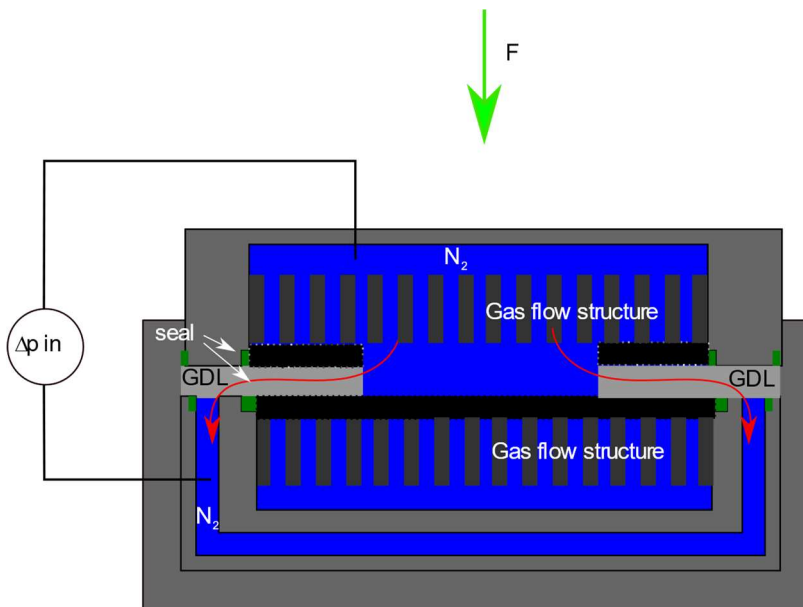


Figure 12: Principle experimental set-up in the in-plane flow arrangement with sample compression.

The in-plane permeability measurement method is calibrated with similar experiments as shown in section 2.1.2.

2.1.4 First results of through-plane and in-plane permeability measurements with sample compression

An exemplary result of a measurement is shown in Figure 13. The gas transport in the plane is considerably better than perpendicular to it. The reason for this is the strong anisotropy in the material. The fibers used have a preferred in-plane direction due to the manufacturing process. The decrease in permeability as a function of mechanical pressure is caused by the compression of the structure, in other words the reduction of porosity. If the porous material surface is hydrophobic and we use water as the medium, there is a higher resistance to the flow. Another effect is that a minimum pressure is necessary for a flow to occur at all. These effects have their origin in the transport of water in hydrophobic capillaries. A general introduction can be found in [13], as well as specific ones in [14] and [15]. The measurements with air and water are carried out in the same apparatus.

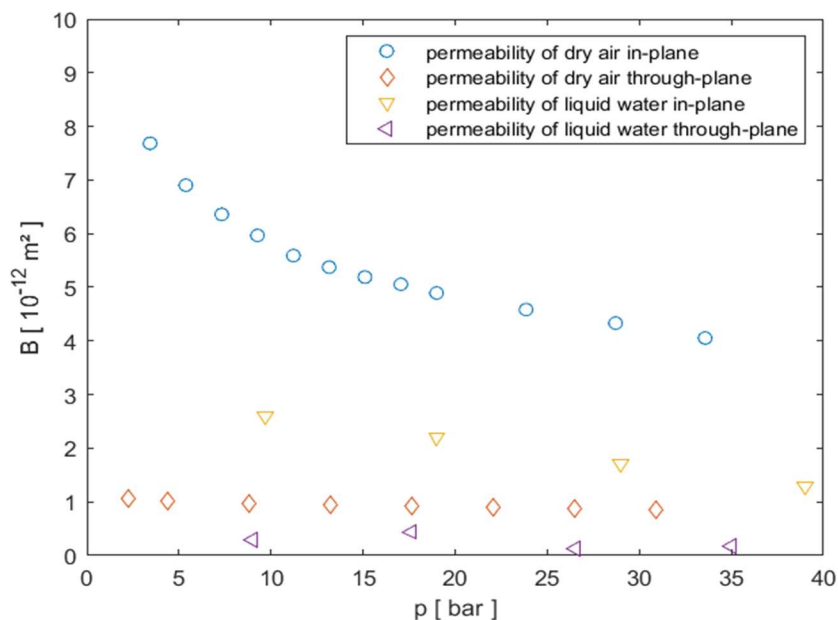


Figure 13: In-plane and through-plane permeability with sample compression of dry air and liquid water.

2.2 Specific in-plane conductivity and contact resistance characterisation technique

The electrical resistance can be divided into two parts, the bulk resistance, and the contact resistance. The bulk resistance is a material property. The contact resistance between two materials is determined both by the choice of these two materials and by the surface properties of the contact surfaces. If two different materials are brought into electrical contact, the different Fermi levels create a barrier that the electrons must overcome [16]. If the surface is dirty or has an oxide layer, this must be considered as well. The contact resistance depends on the roughness of the surface (see Figure 14). The electrical field is constricted at the contact points, causing increased resistance [17]. The smaller the points are, the stronger the constriction of the electrical field and the fewer points have contact, the greater the resistance.

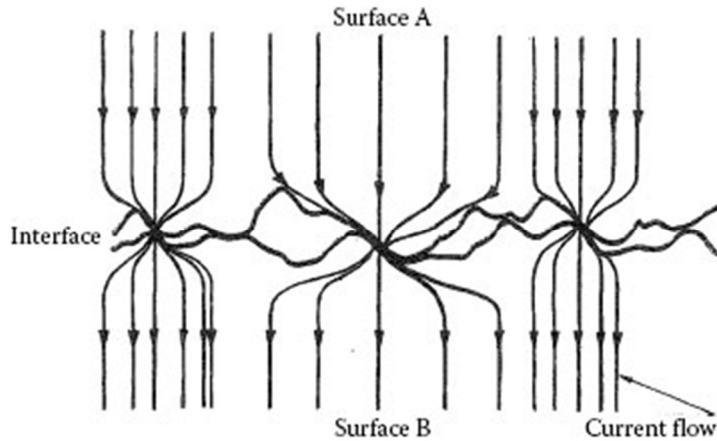


Figure 14: Principal representation of the constriction resistance.

The contact resistance can be determined using different methods, see [16]. The transfer line method (TLM) (or transfer length method) is described here [18]. In this method, contacts are applied to the sample at different distances (d_{nm}). The resistance between the contacts is determined by a current-voltage measurement (see Figure 15).

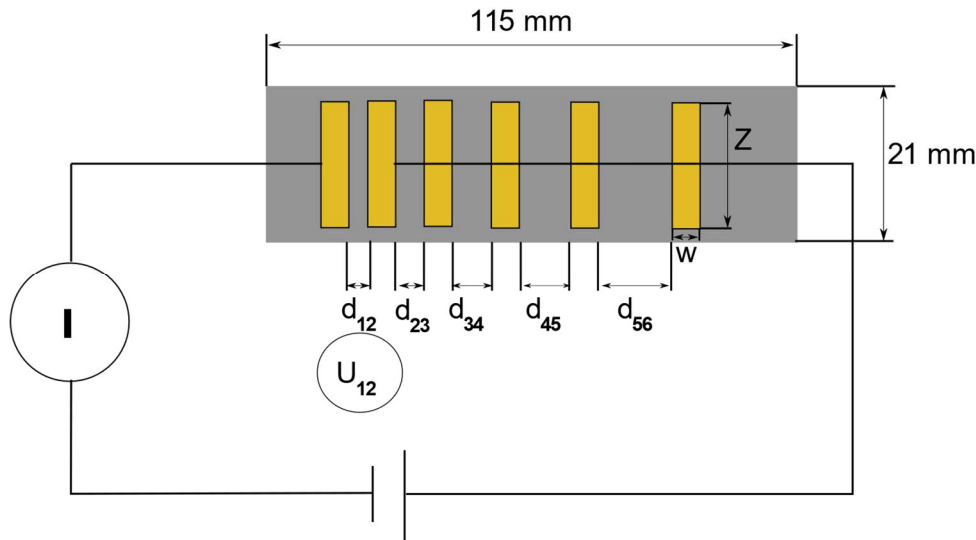


Figure 15: Principal representation of the transfer line measurement method.

The increasing distances result in the following curve of the resistance R_{meas} as a function of the contact distance d_{nm} . It is assumed here that the bulk resistance of the gold platelet is negligibly small. This consideration then results in the following equation:

$$R_{meas} = 2R_C + R_{bulk} \frac{d_{nm}}{Z} \quad (20)$$

The specific in-plane conductivity can be determined from the slope of the linear curve, where t describes the thickness of the sample.

$$\sigma = \frac{Zt}{R_{bulk}d_{nm}} \quad (21)$$

Figure 16 shows that the resistance increases linearly with increasing distance, whereby the resistance is made up by two times contact resistance gold -GDL and the GDL bulk resistance.

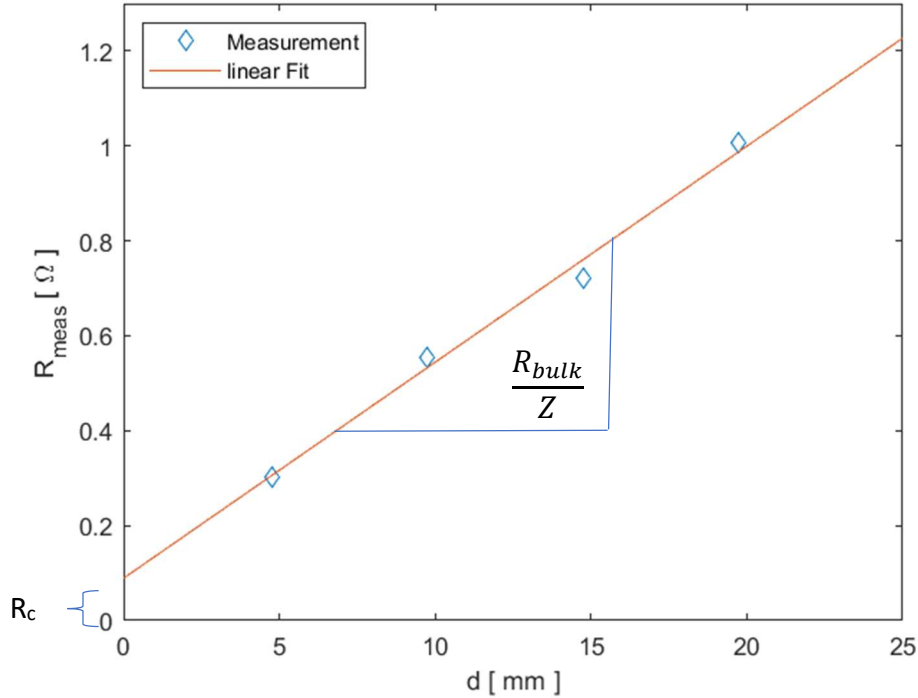


Figure 16: TLM method measurement data and interpretation.

For a more detailed consideration of the electric field under a contact surface [16], the E-field structure under the contact must be considered. For this purpose, a resistance network is set up and the corresponding differential equations are solved (see Fig. 17). A brief calculation gives the following relationship between R_c and the specific contact resistance ρ_c [16], [19].

$$R_c = \frac{\sqrt{R_{bulk}\rho_c}}{Z} \coth\left(\sqrt{R_{bulk}/\rho_c} w\right) \tag{22}$$

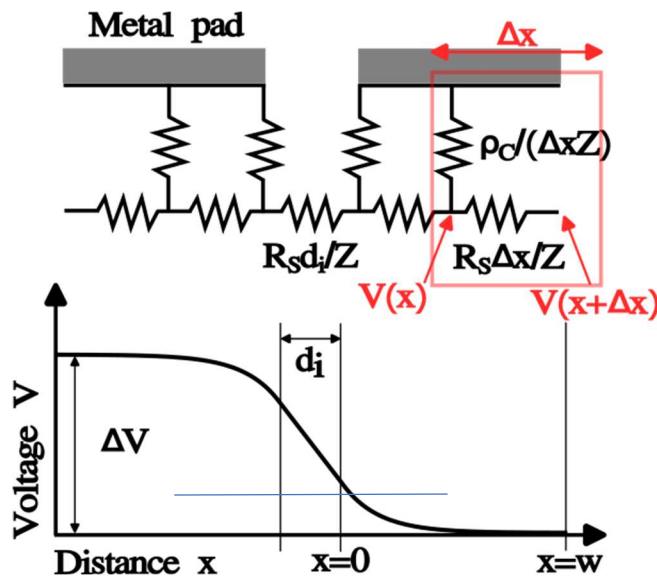


Figure 17: Resistance network considered in TLM method [19].

Figure 18 illustrates the experimental setup with gold electrical contacts (left) and a GDL placed on top of these contacts (right).

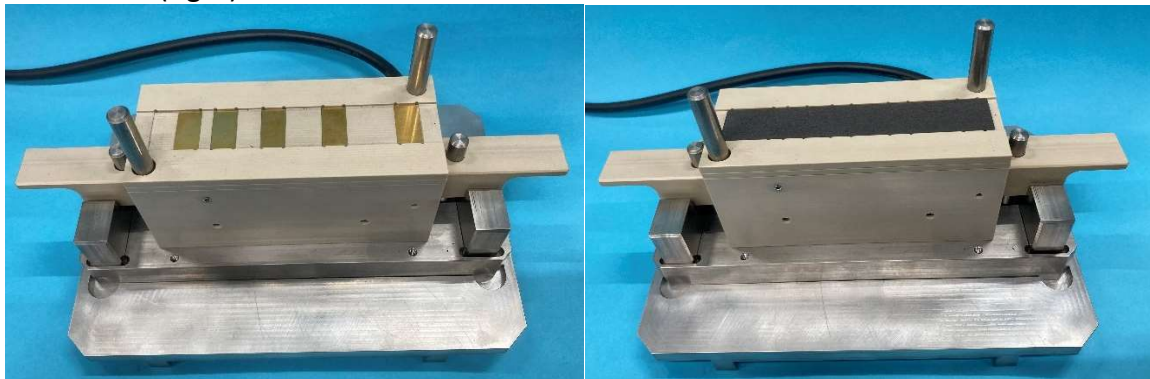


Figure 18: Experimental set-up for TLM.

Figure 19 shows the entire device in the testing machine, which can exert a maximum force of 5 kN corresponding to a mechanical pressure of approximately 50 bar. The device can also be heated up to 150 °C using electric heating cartridges.



Figure 19: Experimental set-up for TLM.

2.2.1 Calibration of the TLM measurement method

As there are no standards for determining the contact resistance, a gold sample was measured instead of the GDL, whose specific conductivity is well known and whose surface and therefore also the contact

resistance do not change over time. The result of the specific conductivity measurement deviates approx. 5% from the literature values (see Figure 20). The main reason for this is the very high conductivity of the Au sample, which is approximately four orders of magnitude greater than the expected conductivity. As expected, the values are almost independent of pressure, the first value being slightly higher because the contact was not yet perfect at this pressure level.

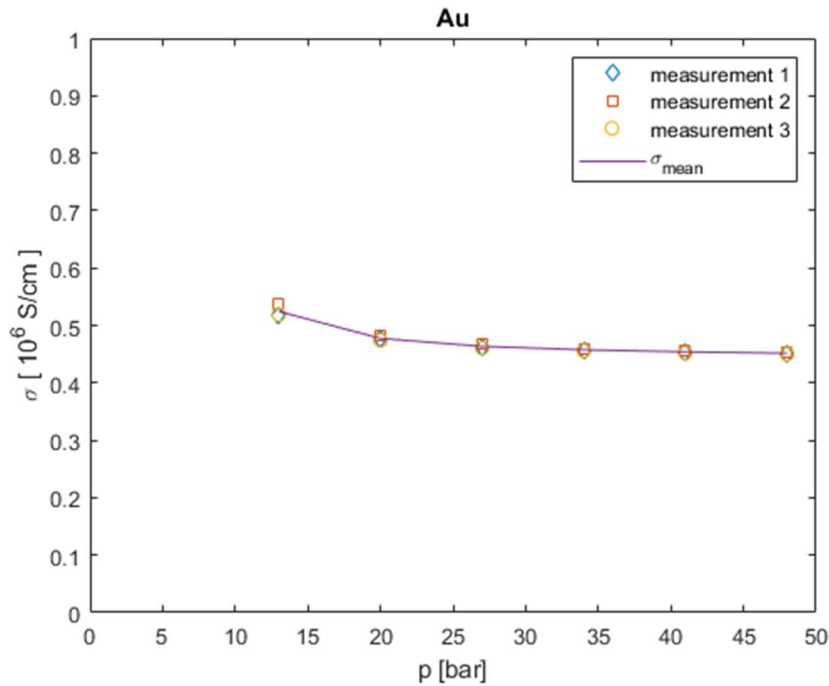


Figure 20: Calibration of the TLM, specific conductivity.

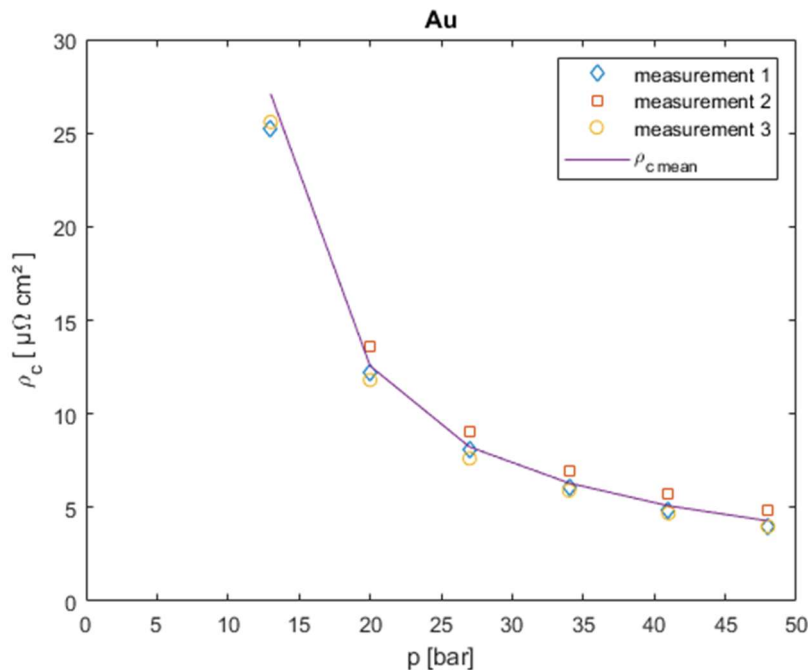


Figure 21: Calibration of the TLM, contact resistance.

The measurement of the contact resistance is shown in figure 21 and indicates a strong dependence on the external pressure. This behaviour can be explained by the increase in contact points (see figure 14 and [17]). The reproducibility of the results can be seen in the figure 22; three measurements were carried

out on the same sample in each case. To investigate the stability of the measurement, the measurement was carried out over 2 h at a pressure point (approx. 40 bar). No change over time occurs within the measurement accuracy.

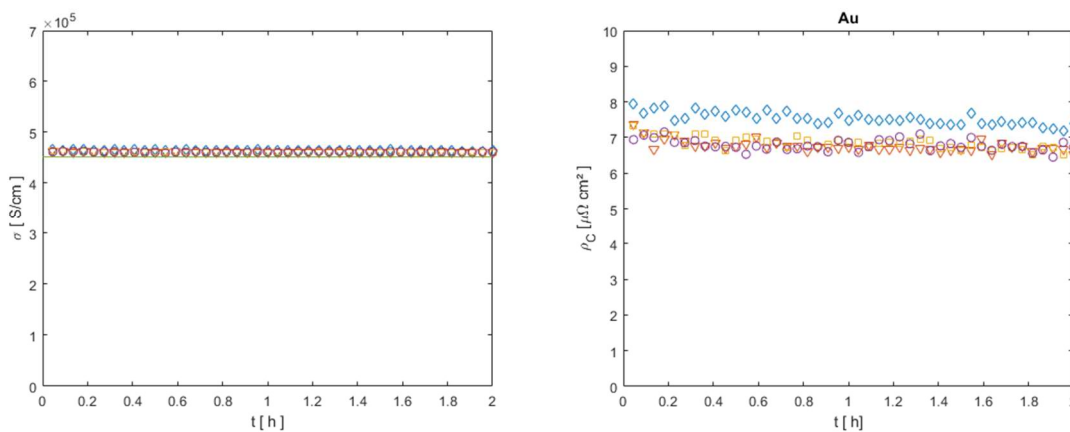


Figure 22: Calibration of the TLM, stability of the measurement.

2.2.2 Results of specific in-plane conductivity and contact resistance measurements.

Two commercial products were measured as the first GDLs to be examined, namely SGL 22BB from SGL Carbon and H15C14 from Freudenberg. The measurements were carried out on five samples each, the range of variation is symbolised by the error bar.

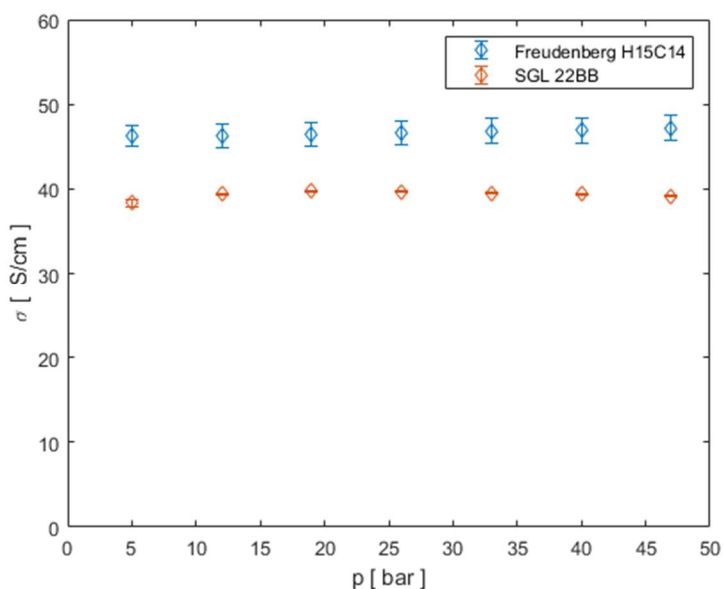


Figure 23: Specific conductivity of different GDLs.

Figure 23 shows the specific conductivity as a function of pressure. The values are almost constant. The differences in conductivity between Freudenberg and SGL GDL are due to the different thermal treatment of the fibres and the different fibre mesh structure.

Figure 24 shows the contact resistance as a function of pressure. The contact resistance of both GDLs decreases with increasing pressure as the number of contact points increases. It plateaus off at higher pressures.

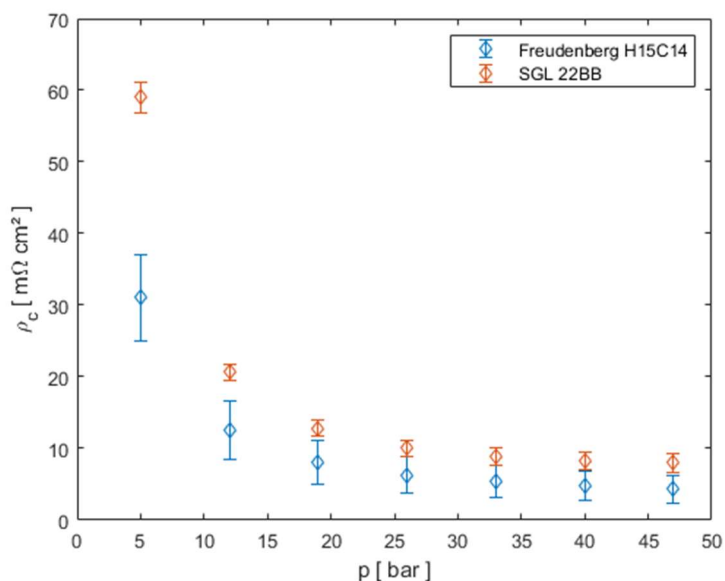


Figure 24: Contact resistance of different GDLs.

2.3 Through-plane resistance measurement method

The through-plane resistance is determined between two gold-plated stamps with a diameter of 30 mm. The stamp itself is installed in a testing machine that can generate a force of up to 5 kN. The measurement is carried out in a 4-point arrangement. The experimental setup can be seen in figure 25.

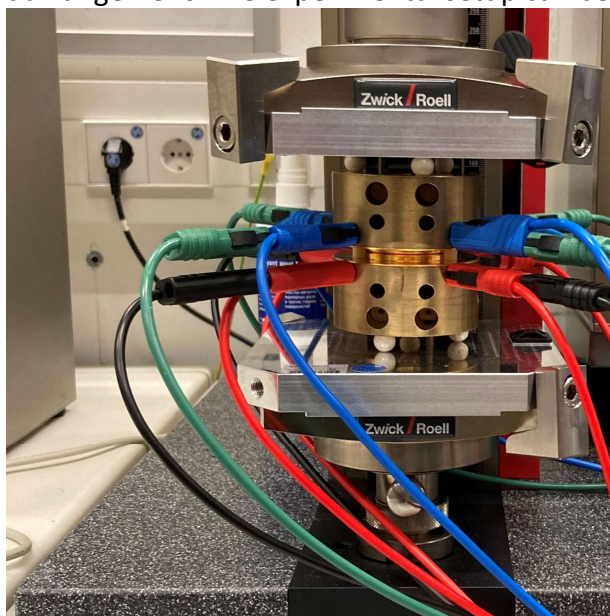


Figure 25: Experimental setup for determining the through-plane resistance.

Figure 26 shows an exemplary measurement result as a function of pressure. The through-plane resistance decreases with increasing pressure as the contact resistance and the bulk resistance both decrease.

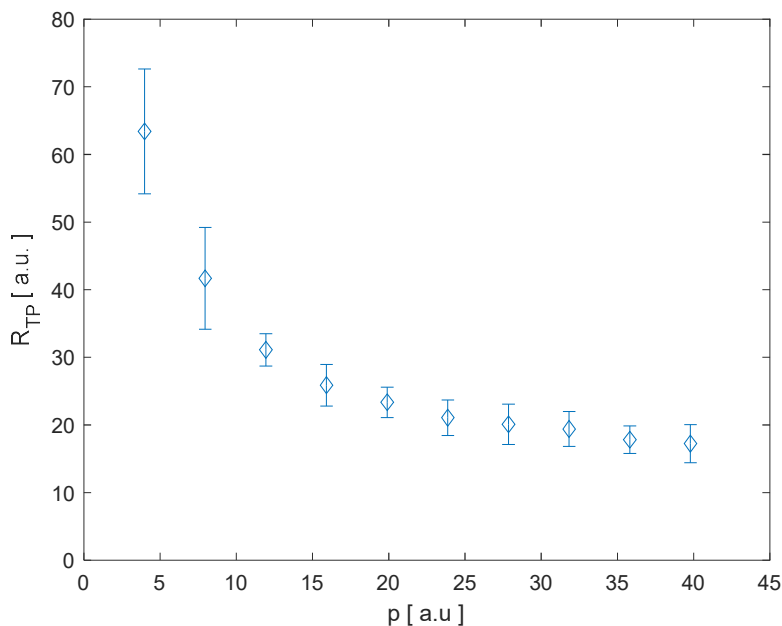


Figure 26: Through-plane resistance as a function of pressure.

3 CONCLUSIONS AND FUTURE WORK

Measurement methods to characterise ex situ GDL properties under mechanical pressure have been developed, implemented, calibrated, and tested for stability:

- a) in-plane and through-plane **permeability**
- b) in-plane and through-plane **bulk resistance**
- c) **contact resistance**

The measurement methods are ready to use and will be applied to characterise HIGHLANDER GDL samples guiding the future design and process development.

4 REFERENCES

- [1] X. Wang and e. al, "Micro-porous layer with composite carbon black for PEM fuel cells," *Electrochimica Acta*, vol. 51, pp. 4909-4915, 206.
- [2] C. H. Ho and S. W. Webb, *Gas Transport in Porous Media*, Dordrecht: Springer, 2001.
- [3] V. Gurau and e. al., "Characterization of transport properties in gas diffusion layers for proton exchange membrane fuel cells 2. Absolute permeability," *Journal of Power Sources*, vol. 165, pp. 793-802, 2007.
- [4] R. Schweiss and e. al., "https://www.sglcarbon.com/en/markets-solutions/material/sigracet-fuel-cell-components/," SGL Carbon GmbH. [Online]. [Accessed 20 11 2019].
- [5] H. Darcy, *Les Fontaines Publiques de la Ville de Dijon.*, Paris: Victor Dalmont, 1856.
- [6] D. A. Nield and A. Bejan, *Convection in Porous Media*, Springer, 2017.

- [7] M. A. Van Doormaal and J. G. Pharoah, "Determination of permeability in fibrous porous media using the lattice Boltzmann method with application to PEM fuel cells," *International Journal for Numerical Methods in Fluids*, vol. 59, pp. 75-89, 2009.
- [8] S. Sharma and D. A. Siginer, "Permeability Measurement Methods in Porous Media of Fiber Reinforced Composites," *Applied Mechanics Reviews*, vol. 63(2), p. 020802, 2010.
- [9] M. L. Huber and A. H. Harvey, CRC Handbook of CHEMISTRY and PHYSICS, Boca Raton, FL: CRC-Press, 2011.
- [10] J. P. Feser and e. al., "Experimental characterization of in-plane permeability of gas diffusion layers," *Journal of Power Sources*, vol. 162, pp. 1226-1231, 2006.
- [11] J. R. Weitzenböck, R. Shenoï and P. A. Wilson, "Radial flow permeability measurement. Part A: Theory," *Composites: Part A*, vol. 30, pp. 781-796, 1999.
- [12] J. R. Weitzenböck, R. Shenoï and P. A. Wilson, "Radial flow permeability measurement. Part B: Application," *Composites: Part A*, vol. 30, pp. 797-813, 1999.
- [13] W. D. H. C. Hall, Water transport in brick, stone and concrete, CRC Press, 2022.
- [14] J. P. Owejan, "Water Transport Mechanisms in PEMFC Gas Diffusion Layers," *Journal of The Electrochemical Society*, vol. 157, pp. B1456-1464, 2010.
- [15] A. Bazylak, "Liquid water visualization in PEM fuel cells: A review," *International Journal of Hydrogen Energy*, vol. 34, pp. 3845-3857, 2009.
- [16] D. K. Schroeder, Semiconductor material and devices characterization, A Wiley- Interscience Publication, 2006.
- [17] R. Holm, Electrical Contacts Theory and Applications, Heidelberg: Springer Verlag, 2010.
- [18] H. Berger, "Contact Resistance and Contact Resistivity," *J. Electrochem. Soc.: Solid State Science and Technology*, vol. 119, pp. 507-5014, 1972.
- [19] T. I. method, "Wikipedia," 3 4 2013. [Online]. Available: https://en.wikipedia.org/w/index.php?title=Transfer_length_method&oldid=1185295236. [Accessed 2 2 2024].
- [20] D. K. Schroeder, Semiconductor material and devices characterization, A Wiley-Interscience Publication, 2006.
- [21] R. Holm, Electrical Contacts Theory and Applications, Heidelberg: Springer Verlag, 2010.